Archiwum Instytutu Techniki Cieplnej Vol. **6** (2019) www.itc.polsl.pl/ArchiwumITC

Numerical modelling of microflow and μPIV measurement in microfluidic cell culture device

Michał Loska [*] [†]
Instytut Techniki Cieplnej, Politechnika Śląska
e-mail: m.loska1305@gmail.com

Key words: microflow, CFD, microfluidics, cell culture, μPIV

Abstract
Microfluidics is a relatively young field of study and production of microfluidic devices still has room for improvement. Microfluidic devices can be found in many applications, especially in biology due to immense capabilities to mimic physiological conditions of a living organism. To make the production more convenient and predict the conditions in designed microdevice CFD modelling can be used. It allows predicting, among the others, flow pattern through microchannels and thermal conditions. It can save expensive and time-consuming trial and error method in microdevice prototyping as a modification of geometry and working conditions is much simpler in CFD modelling. In this work construction of the CFD model of flow through microfluidic cell culture device is presented. To verify the CFD model an analytical solution was used. The CFD model results were very close to analytical ones, the average relative difference between the flow velocity was equal to 2.57%. Analysis of flow field results indicated possible improvement of medicine transport to cell culture chambers. The attempt to use simplified μPIV measurement was also a part of the research. These results were compared to the analytical model, the average relative error was equal to 34.55%. The main purpose of measurement attempt was to gain experience in μPIV measurement so the average relative error value was still tolerable. Thanks to this attempt, useful conclusions were drawn allowing for more accurate measurements in the future.

1 Introduction

1.1 Microfluidic devices

Microfluidic devices are systems of channels, mixers, chambers, valves and pumps that handle very small volumes of fluid. They originate from microelectromechanical (MEMS) devices and one of their

[*]This chapter was prepared as a result of Project Based Learning (PBL) project "Design and fabrication of a microchip as a microfluidic system for human cell culture" at the Institute of Thermal Technology, Department of Energy and Environmental Engineering of the Silesian University of Technology, under the supervision of Dr Ziemowit Ostrowski.

[†]This research was carried out as a part of a project POWR-03.05.00-00-Z098/17-00 co-financed by the European Union under the European Social Fund.

first applications were inkjet print heads. Microfluidic devices are usually manufactured using photolithographic patterning, etching and thin-film deposition. Silicone was the material originally used in MEMS microfluidic devices. Currently, the most often used materials in the manufacturing process are polymers and glass due to their optical transparency and lower costs compared to silicone. Study of a microflow and applications of microfluidic devices are an interdisciplinary field of science. Chemistry and biology are in need of tools that can handle a scale of molecules and particles that are of particular interest for above-mentioned sciences. The small size of a single lab-on-a-chip allows carrying out many parallel experiments at the same time, in a single laboratory experiment. Except that, usage of microfluidic devices reduces the consumption of reagents and energy. Fluid mechanics researchers are interested in the surface tension and electrokinetic phenomena that can overwhelm the gravity and the pressure influence in microchannels. The microflow is usually positioned deep within the laminar region because of very low Reynolds numbers. Nusslet number for fully developed laminar flow is independent of Reynolds and Prandtl numbers (e.g. Nu = 3.66 for a circular cross-section and the constant temperature [1]). As hydraulic diameters of microchannels are very low, convective heat transfer coefficients are consequently significantly high. Additionally, taking into account high surface-to-volume ratio, micro-heat exchangers provide very intense heat transfer, making microfluidic devices interesting for heat transfer discipline. This advantageous process is used among the others in microreactors to provide near isothermal conditions during chemical reactions.

1.2 The μPIV measurement

Micro-particle image velocimetry (μPIV) is particle image velocimetry (PIV) adapted to a microscale. PIV allows measuring whole instantaneous velocity field of fluid flow. PIV is only limited by optical access to an interesting section of flow, the transparency of an examined fluid and suitable measurement devices – mainly a high-speed camera. A process of a PIV measurement comprises adding seed or tracer particles to the examined fluid. The material and the diameter of seed particles must be chosen so the particles do not disturb flow itself and, in the same time, ensure that the movement of seed particles is as close to fluid flow as possible. Next, two images of flow of fluid and seed particles are taken, simultaneously the flow is illuminated with a light sheet in a chosen plane. This ensures that the only visible particles will be those illuminated by the light sheet and grants precise information about the position of measured velocity field plane. The flow is illuminated for a very short time, only when the image is taken. This is done to avoid a blurry image of seed particles due to their movement speed. The time between above-mentioned two images is strictly defined. Having two images allows to determine the displacement of particular seed particles. Knowing the time between two pictures and the seed particles displacement consequently allows to determine velocity field of fluid flow, assuming that the movement of seed particles was the same as fluid flow. A process of a μPIV measurement differs from PIV measurement in some aspects. First of all, there is no place for the light sheet – the whole section of a microflow must be illuminated. Seed particles are too small to effectively dissipate light and because of that fluorescent particles are employed. Fluorescence brings another positive trait – particles emit light with a longer wavelength than the wavelength of excitation light emitted by a laser illuminating a microchannel. The usage of dichroic mirror can be seen in figure 1, which presents a simplified scheme of the measurement station. The mirror, transparent to light emitted by particles, filter out excitation light, which is possible thanks to the wavelength difference. It is important as excitation light is not only absorbed by fluorescent particles but also reflected by microchannel walls. The reflected excitation light may overwhelm light emitted by particles. This reflected light can be seen in figure 1 as an arrow on middle laser ray pointed towards the camera. Lack of light sheet makes all particles visible. Measured velocity field plane is set

by defining a focal plane of a camera, leaving particles outside this plane still visible as blurred dots. These blurred dots create distorting image noise. Its adverse effect is limited by the appropriate selection of the diameter and concentration of seed particles.

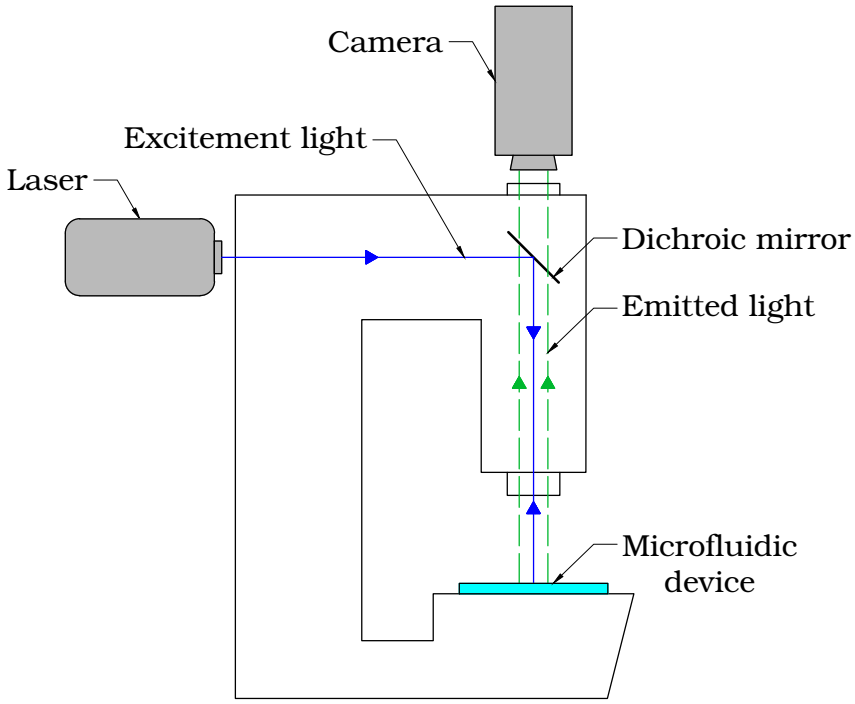

Figure 1: Scheme of a microscope used for a μPIV measurement.

1.3 The purpose and the scope of this work

Biology uses microfluidic devices also to culture cells [2, 3]. The main goal of a project, of which this work is part of, was to fabricate a microfluidic system to culture human cells. The purpose of this work was to create a CFD model of flow through the above-mentioned microfluidic system. One of the additional goals of the main project was an attempt to measure the flow velocity using μPIV method, and attempt to perform μPIV measurement was made as a part of this work. It was done as additional validation, made without a professional μPIV equipment.

2 Analytical model

As stated in the section above, the μPIV measurement resulted in many useful conclusions. Unfortunately, but not surprisingly, the measurement uncertainty, resulting from lack of dedicated measuring devices, software and experience was too significant to use measurement results directly to validate the CFD model. To compensate that, a velocity profile from CFD model was compared to an analytical velocity profile for laminar flow in a rectangular cross-section duct obtained from equations (1) and (2) which can be found in [4].

$$u(y,z) = \frac{16a^2}{\mu\pi^3}\left(-\frac{\mathrm{d}p}{\mathrm{d}x}\right)\sum_{i=1,3,5\ldots}^{\infty}\left\{(-1)^{(i-1)/2}\left[1-\frac{\cosh\left(i\pi z/2a\right)}{\cosh\left(i\pi b/2a\right)}\right]\frac{\cos\left(i\pi y/2a\right)}{i^3}\right\} \tag{1}$$

Where: u, m/s – the local velocity in x direction, x, m – the position on channel length, y, m – the position of the local velocity on channel width, z, m – the position of the local velocity on channel height, a, m – the half of the channel width (as the origin of the coordinate system is in the centre of the channel), b, m – half of the channel height, μ, Pa · s – the dynamic viscosity, p, Pa – the pressure.

$$\dot{V} = \frac{4ba^3}{3\mu}\left(-\frac{\mathrm{d}p}{\mathrm{d}x}\right)\left\{1 - \frac{192a}{\pi^5 b}\sum_{i=1,3,5\ldots}^{\infty}\left[\frac{\tanh\left(i\pi b/2a\right)}{i^5}\right]\right\} \tag{2}$$

Where $\dot{V}$, m^3/s – the volumetric flow rate.

Above equations were successfully used in [5], where velocity profiles of flow through square microchannel acquired from confocal μPIV measurements were compared with an analytical solution. Errors between experimental data and the analytical solution for plane located in the middle of microchannel height, i.e. for $z = 0$, were less than 3%. For planes at $z = 0.3a$ and $z = 0.6a$ errors were, respectively, less than 6% and in the range of 10–13%. As the main interest of this work lies in velocity profile for plane at $z = 0$, good agreement of experimental data and the analytical solution seems to be sufficient to justify verification of the CFD model using those equations.

Equations (1) and (2) were combined into one expression in form of $u = f\left(y, z, \dot{V}\right)$. This operation allowed to exclude $(-\mathrm{d}p/\mathrm{d}x)$ term. As a result, the velocity in a defined location depends on the volumetric flow rate only. As the above equations contain sums of infinite sequences which cannot be expressed in closed-form equation, a numerical solution was proposed (code written in Visual Basic for Applications). In figure 2 an algorithm flowchart of numerical solution is presented. It contains two loops, first is responsible for calculating the series from equation (2), second calculates the series from equation (1). Calculations in the first loop are simple, precision is set to 1E-8 as calculations converge quickly. Second loop demands about ten times more iterations than the first one, yet precision remained equal to 1E-8. This is due to an oscillation of values of subsequent terms of the series. The oscillation results from the presence of cosine. Because of this, not only one term is compared to precision, but also two preceding ones. The largest positive number Excel can handle is equal to ~1E+308. This limits argument of hyperbolic cosine to about 709.9. To avoid errors, if arguments of hyperbolic cosines in equation (1), $\mathrm{k} = i\pi z/2a$ for hyperbolic cosine in the numeral and $\mathrm{l} = i\pi b/2a$ for hyperbolic cosine in the nominative, exceed the value of 705 calculations exit loop. As can be seen, it is an alternative to the condition concerning precision equal to 1E-8. Fortunately, for above-mentioned loop exit for $b/a \in (0.95, 3)$ the last term of the series is smaller than 1E-7, which is still a satisfactory precision. For $b/a \leq 0.95$, which is the case with this work, the premature loop exit does not occur, so precision 1E-8 is met. It is worth noting that the condition concerning argument k is made pro forma – it will never exceed the value of argument l as z may be only equal to or be smaller than b.

3 μPIV measurement results

3.1 Parameters of the measurement

As was mentioned in section 1.2, few factors like the seed particle diameter or the particle concentration must be properly chosen to carry out μPIV measurement. To choose a particle diameter, examples from the literature concerning microchannels with similar dimensions were used. The dimensions of microchannel tested in this work are 150 μm width and 45.5 μm height. In [6] the velocity of flow through a microchannel with 300 μm width and 30 μm height was measured using μPIV method. The diameter

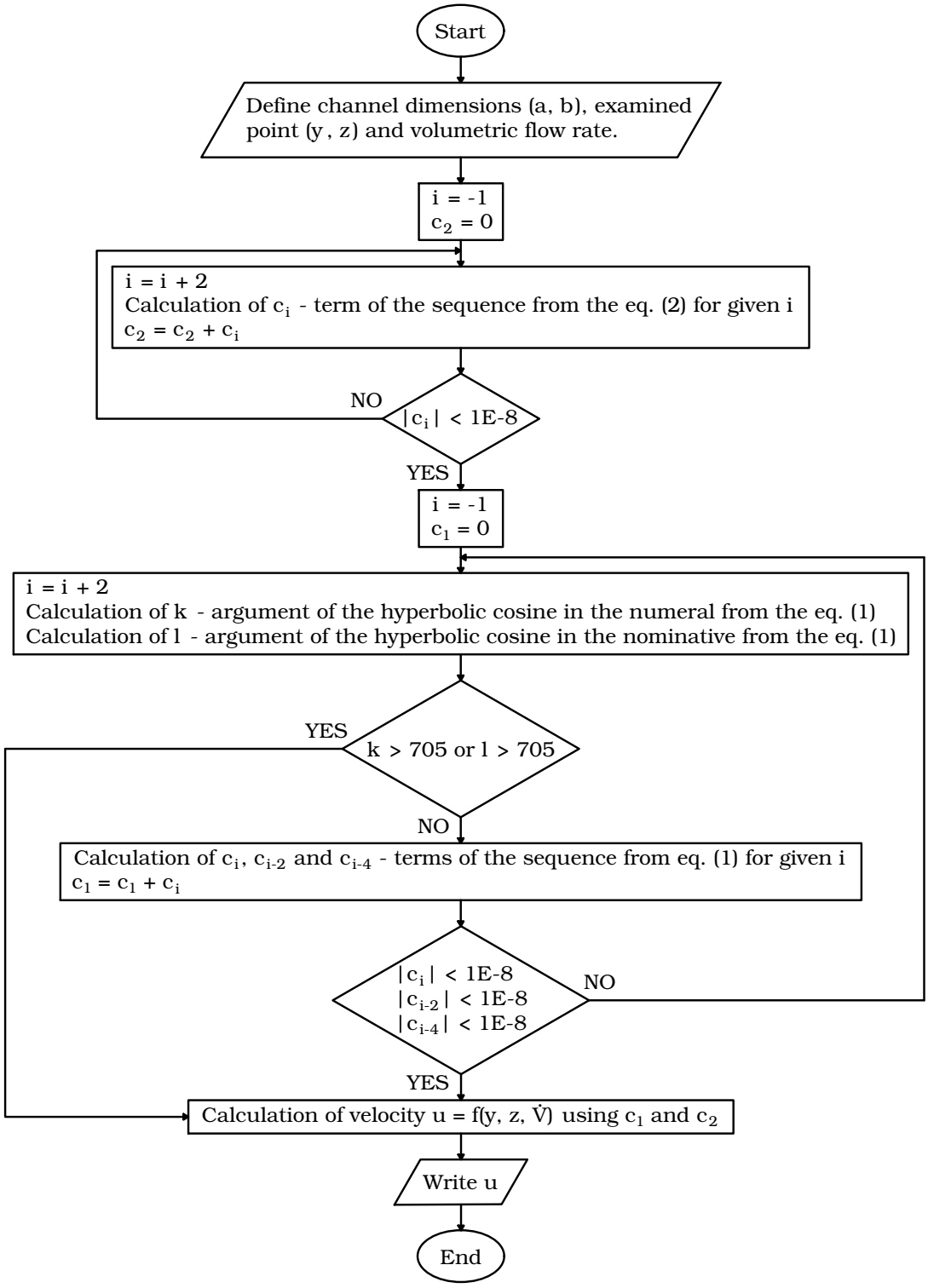

Figure 2: Algorithm flowchart of numerical solution of equations (1) and (2).

of used seed particles was 200 nm. In μPIV measurement carried out in [7] microchannel with 100 μm width and 107 μm height was examined. The diameter of seed particles was 500 nm. Based on diameters

used in above-mentioned works, the diameter of seed particles for μPIV measurement for microchannel tested in this work was selected to be 200 nm. The time between two images (frames), which are used to determine particle displacement, was forced by the frequency of camera that was used (86 Hz). This frequency was limited to 168px x 54px region of interest (ROI). The concentration of seed particles can be estimated using the formula for "visibility" found in [8]. It is defined by the following equation (3)

$$\gamma = \frac{4\mathrm{M}^2\beta^2\left(s_0 - m\right)\left(s_0 - m + H\right)}{\pi c H s_0^2\left\{\mathrm{M}^2 d_p^2 + 1.49(\mathrm{M}+1)^2\lambda^2\left[\left(\frac{\mathrm{n}}{\mathrm{NA}}\right)^2 - 1\right]\right\}} \tag{3}$$

Where: γ, - – the visibility, M, - – the microscope magnification, β, - – the parameter defining a threshold which divides a signal from the noise, s_0, m – the distance between an observed particle and the microscope lens, m, m – the distance between the focal plane and a microchannel wall through which flow is observed, H, m – the microchannel height, c, $1/\mathrm{m}^3$ – the number of seed particles per unit of volume, d_p, m – the diameter of seed particles, λ, m – the wavelength of emitted light by fluorescent seed particles, n, - – the refractive index for a medium between the microscope lens and the microdevice and NA, - – the numerical aperture.

Also in [8] an optimal value of the visibility can be found, which is $\gamma \approx 1.5$. Knowing that and according to equation (3), the number of seed particles per unit of volume c, i.e. concentration of particles, can be estimated. This concentration acquired in the above-mentioned way should be treated as a guess value for the first attempt of a measurement. Then the series of tests for different numbers of seed particles per unit of volume should be carried out to find an optimal value of c. For μPIV measurement, which results were treated below, the number of seed particles per unit of volume was around 0.004 $1/\mu\mathrm{m}^3$. This was the only concentration considered in the measurement. As this measurement was made without proper μPIV equipment, there was no possibility for carrying out further tests to find the optimal value of c. The measurements were conducted for following volumetric flow rates: 500 nl/min, 1000 nl/min, 2500 nl/min, 5000 nl/min.

3.2 Measurement results

The single frame of measurement for the volumetric flow rate equal to 2500 nl/min is presented in figure 3. In figure 4 can be seen a frame for the volumetric flow rate equal to 1000 nl/min. Pictures are in bad quality, mostly due to the low resolution and background noise. Lack of professional μPIV measuring devices forced constant illumination of the examined section of flow. This, in turn, caused seed particles to blur on the pictures to such a degree that only measurement results for the volumetric flow rate equal to 500 nl/min were selected for analysis. The background noise is too significant, additional tests are required to find the optimal concentration of particles. In the initial step, an attempt to use commercial software for traditional, macroscopic PIV. Unfortunately, the quality of images was too bad to process them, even for the volumetric flow rate equal to 500 nl/min. Due to lack of experience in writing code allowing to find centres of particles and compute velocities, the ImageJ software was used instead to obtain measurement results. It required a manual indication of a particle centre on several consecutive frames. In figure 5 the frame after last indication is shown. The circle indicate the location of the examined particle. Eighteen positions of the particle were indicated and, knowing camera frequency, velocity of the particle was calculated. The reliability of results acquired in such a way is limited due to human factor.

Eleven velocities were acquired using ImageJ software and are presented in table 1. The parameter y is the same position as the local velocity on channel width from equation (1) description. The parameter

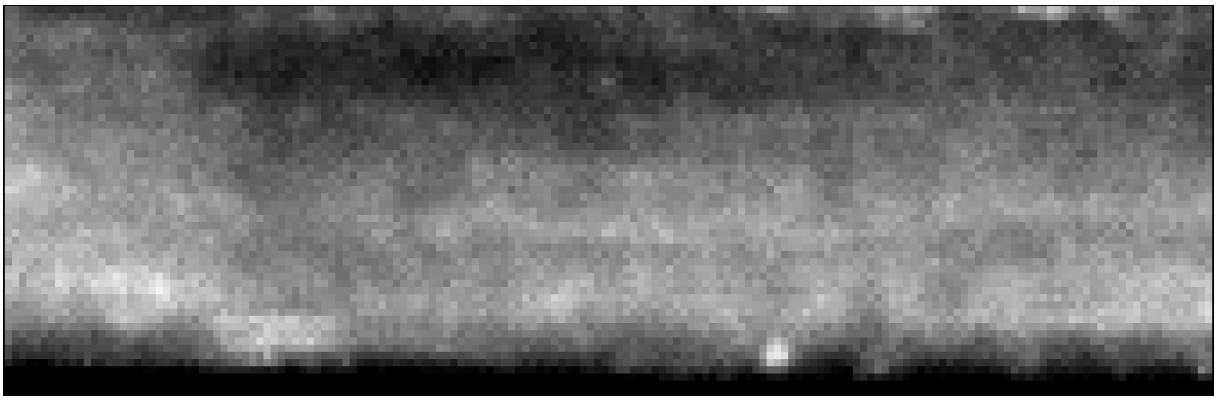

Figure 3: The single frame of measurement for the volumetric flow rate equal to 2500 nl/min.

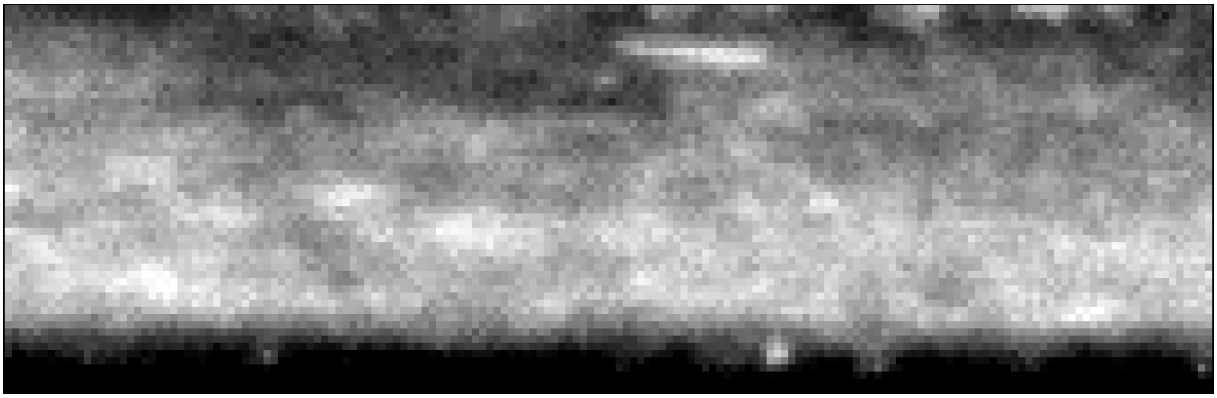

Figure 4: The single frame of measurement for the volumetric flow rate equal to 1000 nl/min.

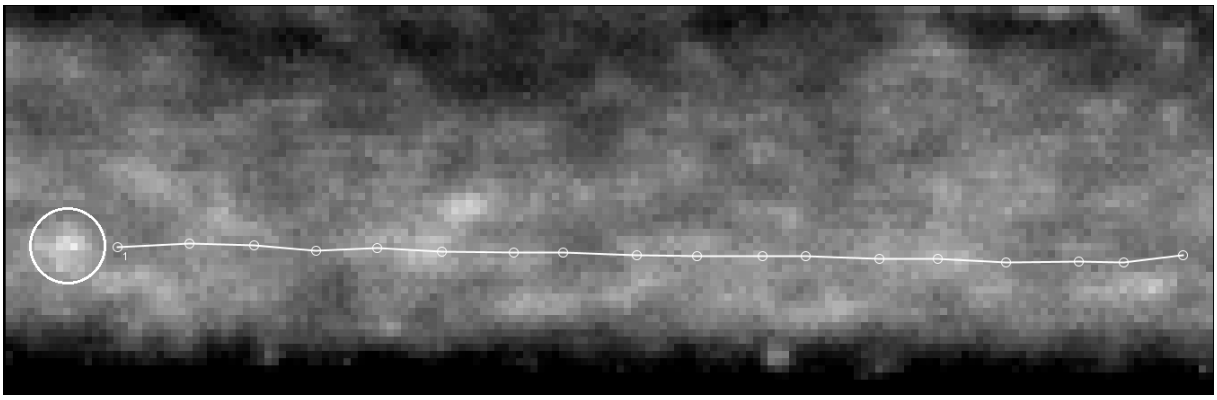

Figure 5: The single frame of measurement for the volumetric flow rate equal to 500 nl/min.

u_{exp} is the measured velocity, u_{am} is the velocity acquired from the analytical model and δ is a relative error between those velocities. Despite the presence of particles with the velocity significantly different from analytical ones, the average of experimental velocities is surprisingly close to the average of analytical velocity – the relative error between them was equal to 34,55%. The error value is still unacceptable for practical use but it is definitely low for measurement results relying on poor quality pictures and human senses.

Table 1: Results of measurement.

No.	y, m	u_{exp}, m	u_{am}, m	δ, %
1	0.0000657	0.003205	0.001046	206.37
2	0.0000455	0.003520	0.001958	79.72
3	0.0000378	0.002326	0.002085	11.57
4	-0.0000141	0.003406	0.002225	53.11
5	-0.0000190	0.002083	0.002212	5.83
6	-0.0000197	0.002079	0.002210	5.92
7	-0.0000208	0.002616	0.002206	18.58
8	-0.0000303	0.003598	0.002156	66.89
9	-0.0000306	0.002190	0.002154	1.66
10	-0.0000361	0.003323	0.002104	57.93
11	-0.0000533	0.001389	0.001743	20.30
Average:	-	0.002703	0.002009	34.55

A graph comparing velocities resulting from the analytical model and experimental velocities is presented in Figure 6. It is a graphical representation of results from table 1. Round dots lying on the line which represents the analytical velocity profile are exact values to which experimental velocities were compared. Looking at near wall experimental velocities with high values it can be concluded that experimental values are overestimated.

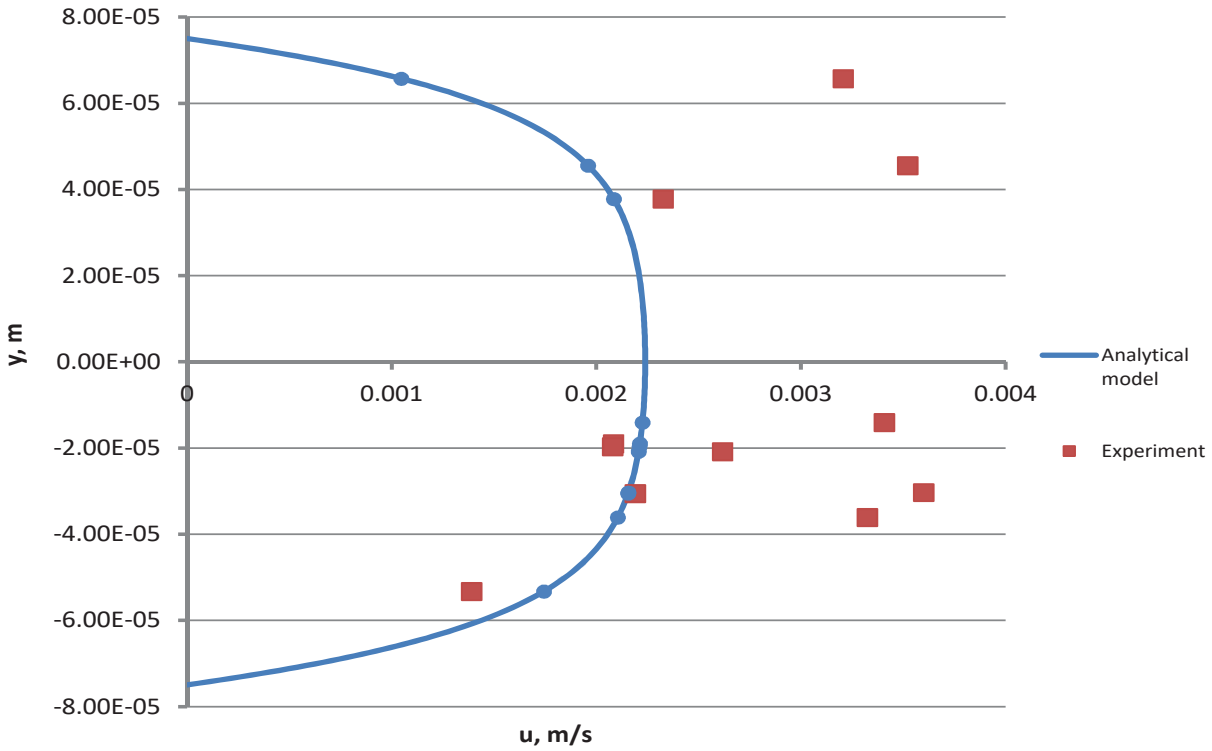

Figure 6: Graphical representation of measurement results.

4 CFD model

4.1 Geometry

The CFD model geometry is shown in Figure 7. It was generated based on a design that was meant to be used in the process of the microdevice fabrication. The geometry consists of twelve cell culture chambers, medicine inlet, mixer and twelve cell culture chambers after the mixer. Cell culture chambers are in the shape of a cuboid. The mixer is resembling a serpentine to intensify mixing process. This is due to the fact that mixing is very slow for low Reynolds numbers which characterise most microflows. The geometry was simplified. Inlets started and outlet ended with an expansion to circle like sockets to which small plastic pipes, with medium or medicine, were connected. These sockets were removed. Sockets were originally fairly far from the main part of microdevice so their removal was insignificant for the flow characteristics. Otherwise, their presence would negatively influence the mesh quality and unnecessarily extend computational time.

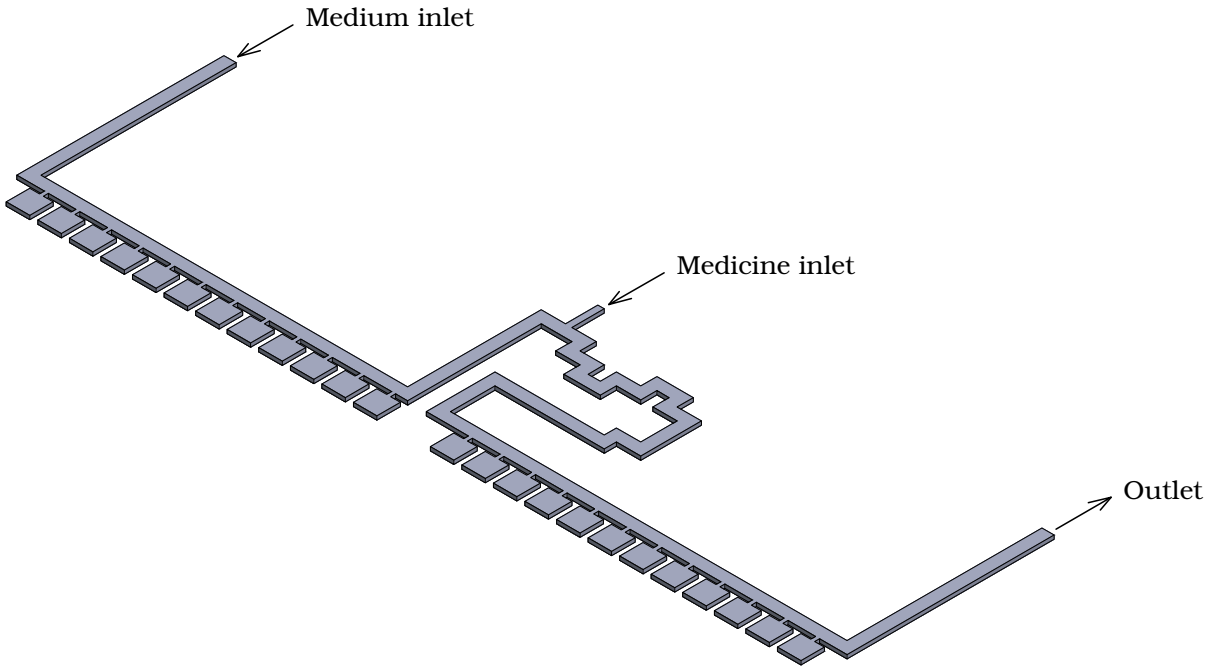

Figure 7: Geometry of the microdevice.

4.2 Grid Convergence Index

Grid Convergence Index (GCI) is a procedure that allows calculating an uncertainty being result of discretisation. Just like in a statistical analysis of measurements, an uncertainty acquired from the GCI procedure defines a range in which the true value can be found with a certain probability – the level of confidence. Calculated uncertainty from GCI procedure corresponds to the level of confidence equal to 95%. Despite above-mentioned similarities to statistical analysis, the GCI procedure does not depend on any probability distribution as the Grid Convergence Index is a semi-empirical method. To compute a discretisation uncertainty using the GCI procedure, iterative convergence must be reached. Lack of iterative convergence causes an iterative uncertainty to appear. The iterative uncertainty distorts the results of

the GCI procedure i.e. the value of discretisation uncertainty. In this work, residuals reached satisfactory low values, as written in section 4.3, so the negligible influence of the iterative uncertainty was assumed. The results of CFD simulation which uncertainties are about to be calculated using the GCI procedure must be in the asymptotic region i.e. meshes used for calculations must be fine enough to provide the independence of the results from the mesh.

In this work, the calculations of the GCI procedure were carried out in accordance with [9]. The first step was to define representative mesh cell size using equation (4):

$$h = \left(\frac{V_{msh}}{\mathrm{N}} \right)^{1/3} \tag{4}$$

Where: h, µm – the representative cell size, V_{msh}, μm^3 – the volume of mesh (the sum of volumes of all cells) and N, – the number of all cells.

Next, the grid refinement factor r was defined. The grid refinement factor is a ratio of the representative cell size of a coarse mesh to the representative cell size of a fine mesh. According to [9] its value should be greater than 1.3. In current work, it was around 1.32.After defining r and choosing the size of cells of the first mesh, the size of cells of other meshes used in the GCI procedure could be calculated.

Then, the apparent (observed) order of convergence j was calculated using set of equations (5), (6) and (7).

$$\mathrm{j} = \left[\frac{1}{\ln(\mathrm{r}_{21})} \right] \left[\ln \left| \frac{\epsilon_{32}}{\epsilon_{21}} \right| + \mathrm{q(j)} \right] \tag{5}$$

$$\mathrm{q(j)} = \ln \left(\frac{\mathrm{r}_{21}^{\mathrm{j}} - \mathrm{s}}{\mathrm{r}_{32}^{\mathrm{j}} - \mathrm{s}} \right) \tag{6}$$

$$\mathrm{s} = 1 \cdot \mathrm{sign} \left(\frac{\epsilon_{32}}{\epsilon_{21}} \right) \tag{7}$$

Where: j, - – the observed order of convergence, r_{21}, - – the grid refinement factor equal to h_2/h_1 where the higher number in subscript denotes the coarser mesh, r_{32}, - – the grid refinement factor analogous to r_{21}, ϵ_{21} and ϵ_{32} – the differences between results of examined variable (variable which uncertainty was being calculated) for given mesh defined by subscript number e.g. $\epsilon_{21} = \omega_2 - \omega_1$ where ω is result of above-mentioned variable.

As can be seen, j is implicit. Equations (5), (6) and (7) were combined into single equation which was numerically solved using Newton's iterative method of solving nonlinear equations. This method requires the derivative of the function which was also acquired numerically using two-point central finite difference method of derivative approximation. The guess value for Newton's iterative method was calculated assuming $\mathrm{q(j)} = 0$ and the precision was set to 1E-5. The finite difference in two-point central finite difference method was set to 1E-6.

Finally, the GCI - Grid Convergence Index i.e. discretisation uncertainty was calculated using equation (8).

$$\mathrm{GCI}_{\mathrm{fine}} = \frac{\mathrm{F_s} \cdot \mathrm{e}_{21}}{\mathrm{r}_{21}^{\mathrm{j}} - 1} \tag{8}$$

Where: $\mathrm{GCI}_{\mathrm{fine}}$, - – discretisation uncertainty for fine mesh i.e. mesh to which corresponds lower number in subscripts of r and e; e_{21}, - – relative error between results of an examined variable and $\mathrm{F_s}$, - – The

Factor of Safety which is equal to 1.25 for analysis involving at least three structured meshes. In other cases it should be equal to 3.

To calculate GCI for the coarsest mesh, equation (9) acquired form [10] must be used.

$$GCI_{coarse} = \frac{F_s \cdot e_{21} \cdot r_{21}^j}{r_{21}^j - 1} \tag{9}$$

As mentioned above, analysis of the independence of the results from the mesh size must be done. In the analysis, six meshes were examined. The parameters compared between meshes were the pressure drop, the friction factor and the mass fraction of medicine in cross-section of an inlet of the first cell culture chamber located after the mixer. The location of the cross-section is shown in figure 8.

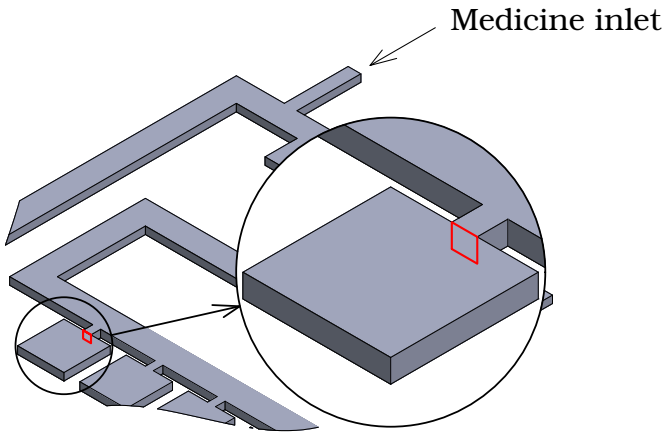

Figure 8: Geometry of the microdevice.

Graphs showing the dependence of the results on the mesh refinement are presented In figure 9. The course of the dependence of the pressure drop Δp and the friction factor f were similar. In the case of the mass fraction of medicine g, the course of dependence on the mesh refinement was much faster convergent. However, the change of absolute values of the mass fraction of medicine was much more drastic than the change of the pressure drop and the friction factor. The mass fraction of medicine value dropped from about 250 ppm to nearly 0. The results for three of the most refined meshes seemed to be in the asymptotic region.

Exact values of the results of the mesh dependence analysis are presented in table 2. Subsequent columns show number of cells, the mass fraction of medicine, the relative difference between the mass fractions in relation to preceding (coarser) mesh, the friction factor, its relative difference analogous to afore-mentioned, the pressure drop, its relative difference analogous to afore-mentioned and finally the computational time. Although the convergence of the pressure drop and the friction factor seemed to be slower than the convergence for the mass fraction of medicine while looking on graphs, the relative differences between results for the pressure drop and the friction factor were relatively low. For the most refined mesh no. 1 the difference was nearly equal to 1%. As the pressure drop and the friction factor are proportional to each other, their relative differences were almost the same. In the case of the mass fraction of medicine, despite good convergence which could be observed in figure 9 the relative differences were relatively high. The greatest relative difference for the coarsest meshes overwhelmed remaining relative differences in figure 9. Good convergence is shown in this figure, but suppressed relative differences of

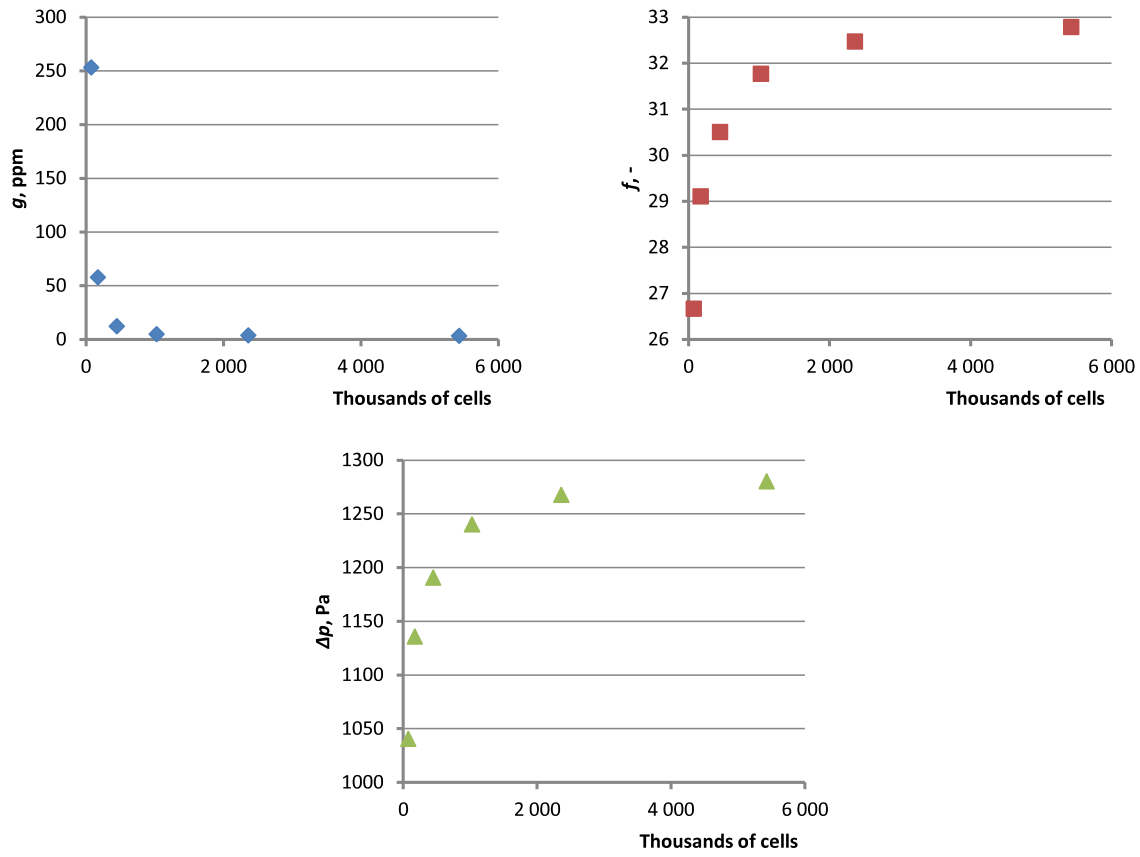

Figure 9: Dependence of the results on the mesh refinement.

the most refined meshes which were apparently still significant as for the finest mesh the relative difference was nearly equal to 12%. Three of the most refined meshes were chosen to be examined in the GCI procedure as the results for them lie in the asymptotic region.

Table 2: The results of the mesh dependence analysis.

No.	N, -	g, ppm	e_g, %	f, -	e_f, %	Δp, Pa	$e_{\Delta p}$, %	t, h
1	5 393 986	3.334	11.91	32.78	0.96	1280.24	0.98	111h 40min
2	2 356 080	3.731	31.00	32.47	2.16	1267.65	2.17	27h 48min
3	1 026 221	4.887	151.07	31.77	3.98	1240.14	3.99	6h 49min
4	392 880	12.270	371.10	30.51	4.59	1190.61	4.61	1h 27min
5	169 976	57.807	337.93	29.11	8.38	1135.70	8.38	0h 23min
6	73 899	253.154	-	26.67	-	1040.52	-	0h 05min

The results of the GCI procedure can be found in table 3. Columns show number of cells, the representative cell size, the grid refinement factor, the examined variable, the observed order of convergence, the relative error between results and the discretisation uncertainty. The discretisation uncertainties for the pressure drop and the friction factor are satisfactory for all examined meshes. Unfortunately, the value of the discretisation uncertainty for the mass fraction of medicine is significantly higher than the discretisation uncertainties for other variables. The best, yet not optimal solution would be the most refined mesh no. 1. The discretisation uncertainty of the mass fraction for the mesh no. 1 was equal to around 8%.

The computations were carried over on the PC unit using two Intel Xeon E5620 2.4 GHz processors. The

Table 3: The results of the GCI procedure.

The mass fraction of medicine							
No.	N, -	h, μm	r, -	g, ppm	j, -	e, %	GCI, %
1	5 393 986	3.59	-	3.334	-	11.91	7.84
2	2 356 080	4.73	1.318	3.731	-	31.00	20.31
3	1 026 221	6.25	1.319	4.887	3.853	-	59.06
The friction factor							
No.	N, -	h, μm	r, -	f, -	j, -	e, %	GCI, %
1	5 393 986	3.59	-	32.78	-	0.96	0.99
2	2 356 080	4.73	1.318	32.47	-	2.16	2.21
3	1 026 221	6.25	1.319	31.77	2.878	-	4.91
The pressure drop							
No.	N, -	h, μm	r, -	Δp, Pa	j, -	e, %	GCI, %
1	5 393 986	3.59	-	1280.24	-	0.98	1.05
2	2 356 080	4.73	1.318	1267.65	-	2.17	2.30
3	1 026 221	6.25	1.319	1240.14	2.814	-	5.01

computational time can be seen in table 2. The computational time equal to almost 112 hours for mesh no. 1 makes the usage this mesh ineffective. As a compromise between uncertainty and computational time mesh no. 2 was chosen. The computational time of 28 h makes the mesh no. 2 much more practical than mesh no. 1. The price for the time was quite substantial as the discretisation uncertainty rose from 8% to 20% but it was still acceptable. The visual comparison between meshes no. 1 and 2 can be seen in figure 10. As can be seen, the condition concerning the structure of a mesh was met. The fulfilment of which allowed using The Factor of Safety equal to 1.25.

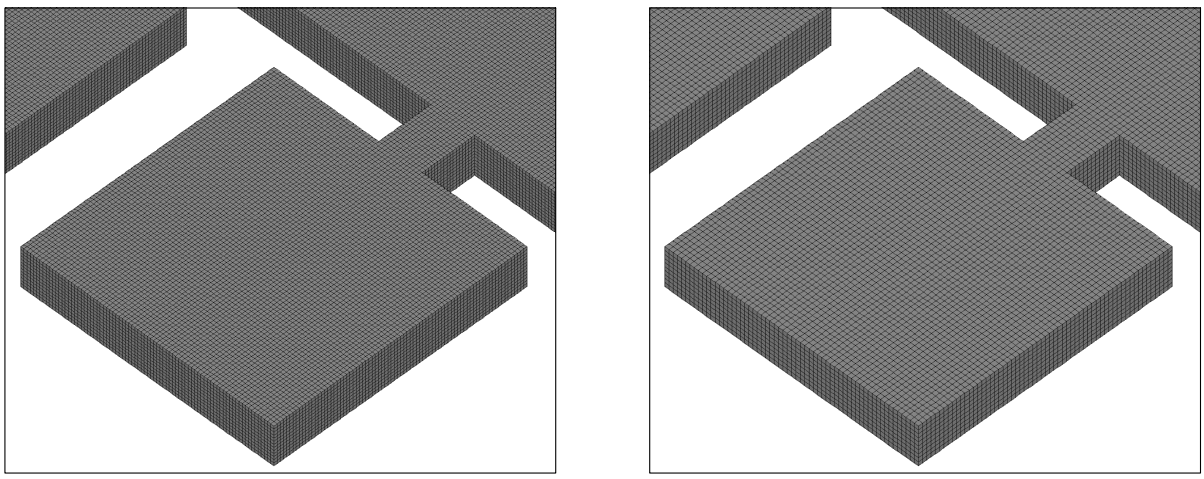

Figure 10: Visual comparison of meshes no. 1 and 2.

4.3 Solver set up

This section describes settings of solver, used materials and boundary conditions. As flow through the microdevice was laminar, a laminar viscous model was chosen. There was no need to turn on the energy equation as the flow was assumed to be isothermal. To capture the flow of the medium and the

medicine, species transport was used. The properties of the medium and the medicine was assumed to be the same as water. The microdevice simulates physiological conditions, so the temperature for which properties were taken was equal to 37°C. Thus the density of the medium and the medicine was set to 993.272 kg/m^3 according to [11]. To calculate mixture density, volume weighted mixing law was used and the mixture dynamic viscosity was set to 6.9254E-4 $Pa \cdot s$ [11]. During the project, the decision on the choice of the type of medicine has not been resolved. Because of that, the mass diffusivity of the mixture, using constant dilute approximation, was set to 1E-9 which characterises caffeine, according to [12]. The examined volume flow of medium was 5000 nl/min, so the boundary condition for the medium inlet was set as velocity inlet with the velocity magnitude equal to 0.01221001 m/s. For the medicine inlet, the velocity inlet with the velocity magnitude equal to 0.0002289377 m/s as the volume flow of medicine was 500 nl/min. The outlet was set as a pressure outlet. The under-relaxation factors were left default except for the one for medicine species. It was reduced from 1 to 0.8 to provide deeper convergence. At the end of calculations, the residuals reached values for continuity, x-velocity, y-velocity, z-velocity and the medicine species respectively 3E-11, 5E-15, 5E-15, 6E-15 and 2E-12.

4.4 Results

Most of the numerical results were presented in section 4.2 in table 3. In this section field results and comparison between the CFD model and the analytical model will be presented. In figure 11 a graph with afore-mentioned comparison can be seen. As expected, the more refined mesh the more close the CFD results are to the analytical ones. For mesh no. 1 the relative difference between maximal velocities for the analytical model and the CFD model was equal to 2.33%. The relative difference for mesh no. 2 was equal to 2.51%. The average relative difference, calculated in the same way as in table 1, was for mesh no. 1 and 2 equal to 2.28% and 2.57%, respectively. The number of relative differences were averaged based on the mesh density. For mesh no. 1 the number was equal to 31 and for mesh no. 2 it was equal to 25. Due to relatively low differences, the mesh no. 2 proved to be an acceptable choice.

In figure 12 the velocity field results can be seen. The inlet of the microchannel with the first twelve cell culture chambers was omitted as the results for them would insignificantly differ from presented ones. Presented field results reflect the above-mentioned velocity profiles. Additionally, local velocity decrease can be observed near inlets to the cell culture chambers. It was caused by the increase of channel cross-section, which is consistent with the continuity equation.

The mass fraction of medicine concentration field results can be seen In figure 13. Here also the same part of microchannel was omitted as it was the part through which the medicine did not flow. Also, most of the mixer is blank as it comprises medicine inlet. In this inlet, the mass fraction of medicine was equal to 1. To make results visible in an interesting part of microchannel, i.e. channel connected to the cell culture chambers, the scale was limited to 0.08. In the blank part of the mixer, the mass fraction of medicine exceeded afore-mentioned limit. As can be seen, the highest values of the mass fraction were near the microchannel wall opposite to cell culture chambers. This is mostly due to medicine inlet position and probably also due to flow acceleration at tips of sharp turns of microchannel which are visible in figure 12. It is a disadvantageous phenomenon that reduces the effectiveness of the medicine transport to the cell culture chambers.

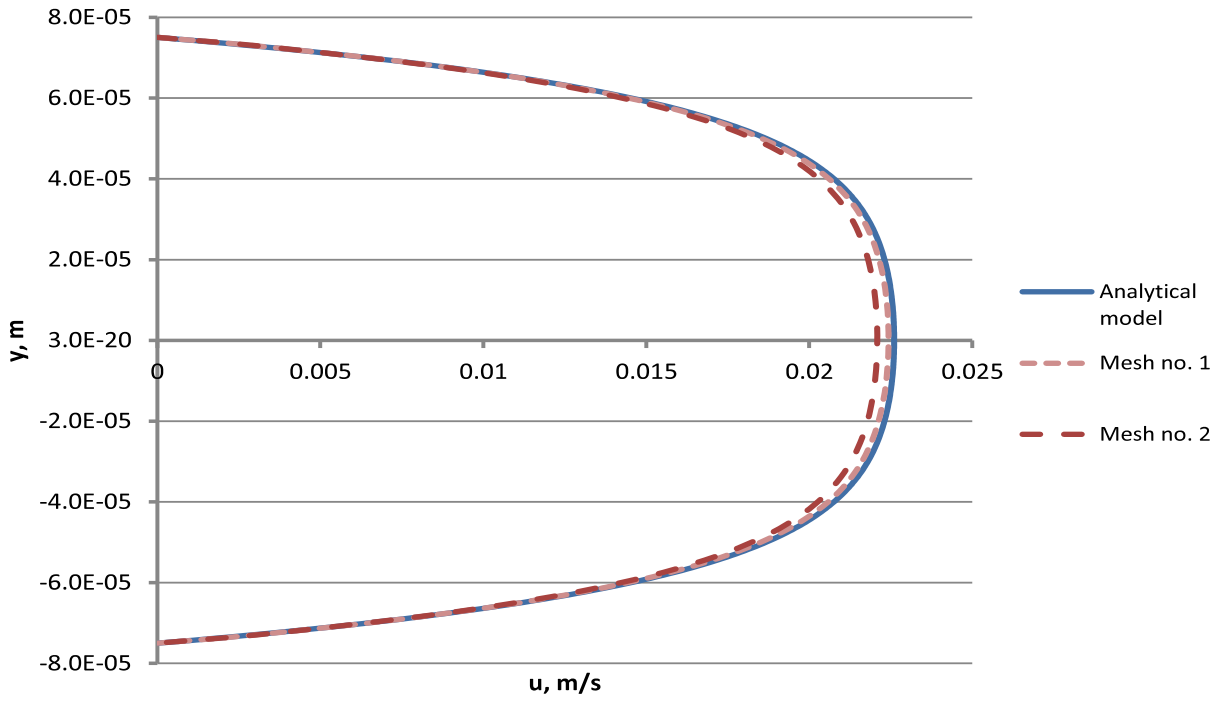

Figure 11: Velocity profiles for the analytical model and the CFD model.

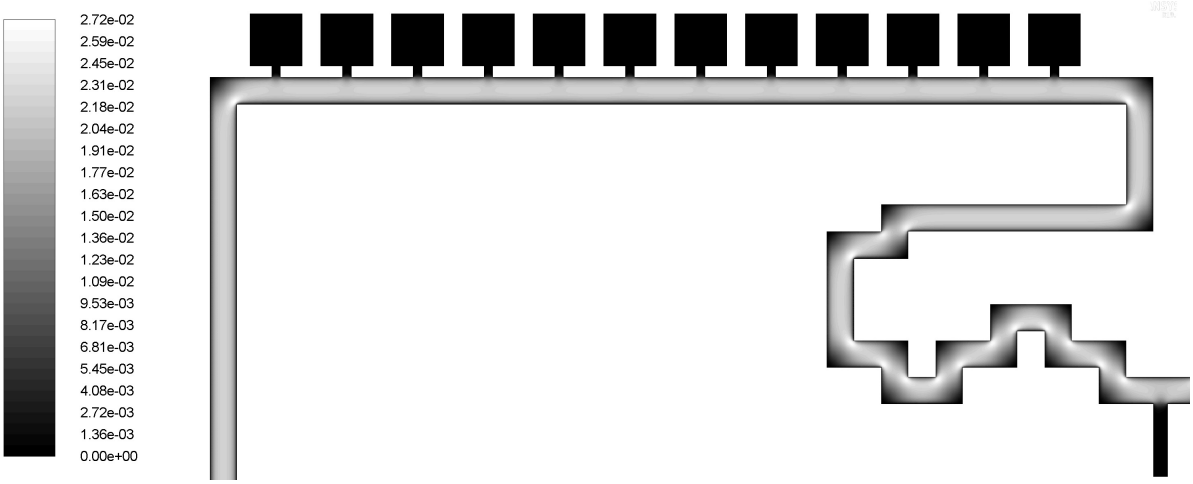

Figure 12: Field results of the velocity in m/s.

5 Conclusions

In this work an analytical model allowing to calculate velocity profile of flow through the rectangular channel was created, simplified μPIV measurement was conducted and a CFD model of flow through microdevice was created.

As the μPIV measurement was only an attempt, its results could not be used for CFD model validation. To verify the CFD model the analytical model was created. It was based on equations acquired from

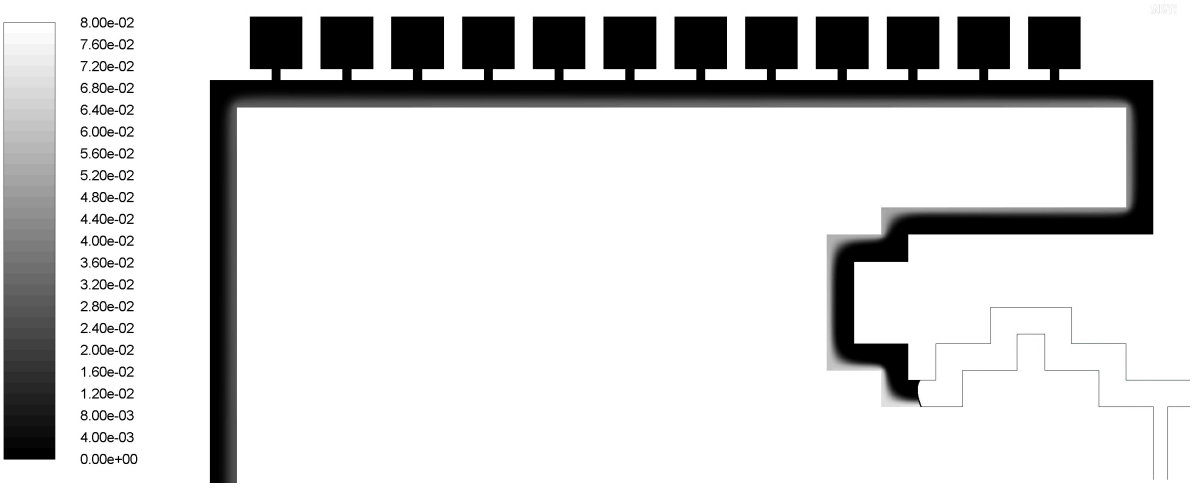

Figure 13: Field results of the mass fraction of medicine.

literature and its calculation results were proven precise in other studies. In this work, the analytical model was also used to check results of μPIV measurement.

The results were acquired using camera unsuited for μPIV and software that required a manual finding of particle centre. Looking at these limited resources and lack of experience in μPIV measurement, the average relative error between results and analytical model equal to 34.55% was tolerable. Of course for practical use it was insufficient but examined measurement attempt indicated area for improvement. First of all the best improvement would be provided by employing a camera dedicated to μPIV as the low resolution of pictures was one of the main problems. This solution is, unfortunately, connected with a substantial expense. Another significant problem was intensive background noise. It can be amended by running a series of tests for different seed particle concentrations in order to find the optimal one. To provide sharp image of particles, continuous illumination of microchannel must be replaced by flashes of laser in the moment of taking the image.

In the creation of the CFD model, the GCI procedure was used. It was used to compute the discretisation uncertainty. The knowledge of discretisation uncertainty value was helpful while choosing a proper mesh. From three meshes, which refinement ensured the independence of results from mesh density, mesh no. 2 was chosen. The mass fraction of medicine in cross-section of cell culture chamber inlet was one of the examined variables. The mass fraction of medicine was the variable characterised by the highest discretisation uncertainty. In case of uncertainty, mesh no. 1 was the best choice as the uncertainty value for the mass fraction was equal to 7.84%. This uncertainty for mesh no. 2 was equal to 20.21%. In case of practicality the mesh no. 2 was the preferable choice as the computational time for mesh no. 2 was about 28 hours. The computational time for mesh no. 1 was around 112 hours. In this work mesh no. 2 was used, but for future work that would demand lower uncertainty, running calculations on the more powerful machine that allows using mesh no. 1 with acceptable computational time could be a solution. The velocity profiles acquired form CFD computations were compared with the analytical ones. For both mesh no. 1 and mesh no. 2 the average relative difference between the CFD velocity profile and analytical velocity profile was satisfactory. For mesh no. 1 the average relative difference was equal to 2.33% and for mesh no. 2 it was equal to 2.57%. It proves that choosing mesh no. 2 was sufficient to at least acquire accurate velocity profile. The mass fraction of medicine field results revealed that the highest values of the examined variable can be found near the wall opposite to the cell culture chambers. It makes the

transport of medicine to the cell culture chambers less effective. The position of medicine inlet seems to be the main reason for that. Placing the inlet on the opposite side of microchannel could solve this problem.

Acknowledgements

This research was carried out within the Project Based Learning (PBL) project as a part of a project POWR-03.05.00-00-Z098/17-00 co-financed by the European Union under the European Social Fund.

I would like to express my deepest gratitude to dr Ziemowit Ostrowski for his advice and availability throughout and after the duration of this project. I would also like to extend my sincere thanks to the whole PBL team for flawless cooperation and good time spend on working together on the project.

References

[1] Y. A. Çengel, A. J. Ghajar, *Heat and Mass Transfer: Fundamentals and Applications*, 5th Ed., McGraw-Hill Education, New York (2015).

[2] P. J. Hung, P. J. Lee, P. Sabounchi, R. Lin, L. P. Lee, *Continuous perfusion microfluidic cell culture array for high-throughput cell-based assays*, Biotechnology and Bioengineering, **89**(1), (2005), pp. 1–8.

[3] R. Gómez-Sjöberg, A. A. Leyrat, D. M. Pirone, C. S. Chen, S. R. Quake, *Versatile, Fully Automated, Microfluidic Cell Culture System*, Analytical Chemistry, **79**(22), (2007), pp. 8557–8563.

[4] F. M. White, *Viscous Fluid Flow*, 3rd Ed., McGraw-Hill, New York (2006).

[5] R. Lima, S. Wada, K. ichi Tsubota, T. Yamaguchi, *Confocal micro-PIV measurements of three-dimensional profiles of cell suspension flow in a square microchannel*, Measurement Science and Technology, **17**(4), (2006), pp. 797–808.

[6] C. D. Meinhart, S. T. Wereley, J. G. Santiago, *PIV measurements of a microchannel flow*, Experiments in Fluids, **27**, (1999), pp. 414–419.

[7] S. Devasenathipathy, J.G. Santiago, S.T. Wereley, C.D. Meinhart, K. Takehara, *Particle imaging techniques for microfabricated fluidic systems*, Experiments in Fluids, **34**, (2003), pp. 504–514.

[8] K. S. Breuer (Ed.), *Microscale Diagnostic Techniques*, 1st Ed., Springer-Verlag, Berlin, Heidelberg (2005).

[9] *ASME V&V 20-2009 Standard for Verification and Validation in Computational Fluid Dynamics and Heat Transfer*, The American Society of Mechanical Engineers, New York (2009).

[10] P. J. Roache, *Perspective: A method for uniform reporting of grid refinement studies*, Journal of Fluids Engineering, **116**(3), (1994), pp. 405–413.

[11] VDI Gesellschaft (Ed.), *VDI Heat Atlas*, 2nd Ed., Springer-Verlag, Berlin, Heidelberg (2010).

[12] W. E. Price, K. A. Trickett, R. K. Kenneth, *Association of caffeine in aqueous solution. Effects on caffeine intradiffusion*, Journal of the Chemical Society, **85**(10), (1989), pp. 3281–3288.

Modelowanie numeryczne mikroprzepływu i pomiar μPIV w mikroprzepływowej hodowli komórek

Michał Loska

Instytut Techniki Cieplnej, Politechnika Śląska
e-mail: m.loska1305@gmail.com

Słowa kluczowe: mikroprzepływ, CFD, mikrourządzenie, hodowla komórek, μPIV

Streszczenie

Badania nad urządzeniami mikroprzepływowymi to stosunkowo młoda dziedzina nauki, a w produkcji urządzeń mikroprzepływowych wciąż jest miejsce na poprawę. Urządzenia mikroprzepływowe znajdują wiele zastosowań, zwłaszcza w biologii ze względu na ogromne możliwości w naśladowaniu warunków fizjologicznych żywego organizmu. Aby ułatwić produkcję i przewidzieć warunki panujące w projektowanym mikrourządzeniu, można zastosować modelowanie CFD. Pozwala ono przewidzieć m.in. warunki przepływu przez mikrokanały oraz warunki termodynamiczne w nich panujące. Modelowanie CFD pozwala zaoszczędzić na kosztownej i czasochłonnej metodzie prób i błędów w produkcji mikrourządzeń, ponieważ modyfikacja geometrii i warunków pracy jest znacznie prostsza w modelowaniu CFD. W tej pracy przedstawiono konstrukcję modelu CFD przepływu przez mikroukład w systemie mikroprzepływowej hodowli komórek. Aby zweryfikować model CFD, skonstruowano model analityczny. Wyniki modelu CFD były bardzo zbliżone do wyników analitycznych, ponieważ średnia względna różnica między profilami prędkości przepływu wynosiła 2,57%. Analiza wyników polowych wskazała na możliwą poprawę efektywności dostarczenia leku do komór hodowlanych. Opracowanie wyników próbnego pomiaru μPIV było również częścią tego badania. Po opracowaniu wyników, porównano je z wynikami modelu analitycznego - średni błąd względny wyniósł 34,55%. Głównym celem próbnego pomiaru było zdobycie doświadczenia w pomiarze μPIV, więc średnia wartość błędu względnego była nadal dopuszczalna. Dzięki tej próbie wyciągnięto użyteczne wnioski pozwalające na dokładniejsze pomiary w przyszłości.